Aerosol radiative forcing over east Asia determined from ground-based solar radiation measurements

Do-Hyeong Kim[1] and B. J. Sohn
School of Earth and Environmental Sciences, Seoul National University, Seoul, Korea

Teruyuki Nakajima
Center for Climate System Research, University of Tokyo, Tokyo, Japan

Tamio Takamura
Center for Environmental Remote Sensing, Chiba University, Chiba, Japan

Received 23 February 2004; revised 16 June 2004; accepted 9 September 2004; published 18 March 2005.

[1] We developed a method of retrieving aerosol optical properties and their associated radiative forcing from simultaneously measured sky radiation and surface solar flux data. The method is then applied to data sets collected at Mandalgovi, Dunhuang, Yinchuan, and Sri-Samrong sites of the Skyradiometer Network (SKYNET), and at Anmyon, Gosan, and Amami-Oshima, to examine the aerosol characteristics of east Asia. From the analysis for the SKYNET sites it was found that aerosols in east Asia have smaller single scattering albedos (i.e., 0.89 for Asian dusts in Dunhuang, 0.9 for urban type aerosols in Yinchuan, and 0.88 for biomass burning aerosols in Sri-Samrong), compared to the single scattering albedo for the same type of aerosols found in other areas. Lower single scattering albedo suggests that the aerosols over east Asia absorb comparatively more solar radiation. The measurements taken during April at the latter three sites over the Korean peninsula and the East China Sea showed that the single scattering albedo of Asian dust becomes smaller during the course of its movement from the source region to east Asian seawaters (i.e., 0.86 at Anmyon, 0.84 at Gosan, and 0.80 in Amami-Oshima), compared with 0.89 found in the source region (i.e., Dunhuang). These findings strongly suggest that Asian dusts become blackened during the movement because of mixing with soot particles produced over the industrial/urban area of China. The overall atmospheric forcing efficiency (radiation flux per unit aerosol optical thickness at 0.5 μm) of Asian dusts ranges from 65 to 94 W m^{-2} near the east Asian seaboard area, indicating that atmospheric heating by Asian dusts can be significantly enhanced by the mixing with soot particles.

Citation: Kim, D.-H., B. J. Sohn, T. Nakajima, and T. Takamura (2005), Aerosol radiative forcing over east Asia determined from ground-based solar radiation measurements, *J. Geophys. Res.*, *110*, D10S22, doi:10.1029/2004JD004678.

1. Introduction

[2] It is well known that one of the major problems of contemporary climate research in diagnosing climate change and in climate change prediction is the role of aerosols in maintaining and modulating the global radiation balance. This is due to radiation energy being the ultimate forcing inducing global circulation; thus changes in radiative energy due to anthropogenic aerosols can have an impact on the global climate [*Haywood and Boucher*, 2000; *Ramanathan et al.*, 2001a]. Despite the importance of aerosols in the study of global climate change, our understanding is so far very limited, because aerosol radiative forcing (ARF) is large but of uncertain magnitude [*Haywood and Ramaswamy*, 1998; *Jacobson*, 2001]. Considering that our understanding of the role of aerosols in the radiative forcing at the top of the atmosphere (TOA) is much low, in comparison to our understanding of CO_2 influences [*Intergovernmental Panel on Climate Change* (*IPCC*), 2001], it is difficult to assess man-made influences on the climate without accurate measurement of aerosol induced radiative forcing. Accordingly, as reported in the work of *IPCC* [2001], the uncertainties in radiative forcing induced by aerosols should be resolved in order to accurately estimate or predict the man-made impact on our climate system.

[3] In line with these needs, there have been efforts to quantify the magnitude of ARF and its impact on the local

[1]Now at Scripps Institution of Oceanography, University of California, San Diego, La Jolla, California, USA.

0148-0227/05/2004JD004678$09.00

and global climate. The Indian Ocean Experiment (INDOEX; *Ramanathan et al.* [2001b]) quantified direct and indirect aerosol forcing from the measurements of aerosol optical properties and radiation over the Indian Ocean. They found that large ARF efficiencies (radiation flux per unit aerosol optical thickness at 0.5 μm) of -75 W m^{-2} and -25 W m^{-2} at the surface and TOA, respectively [*Satheesh and Ramanathan*, 2000]. *Chung et al.* [2002] showed that the haze radiative forcing imposed by the values obtained during the INDOEX, leads to increased precipitation over the haze area by as much as 20%.

[4] In east Asia, in order to determine the physical, chemical, and radiative properties of aerosols, as well as to quantify aerosols-radiation interactions, the Asian-Pacific Regional Aerosol Characterization Experiment (ACE-Asia) was conducted over the East China Sea [*Huebert et al.*, 2003]. The physical and chemical processes controlling the evolution of the major aerosols were also studied. The results of ACE-Asia have shown that dusts in Asia can be transported half way around the globe, and air pollution can significantly change dust aerosols by adding black carbon, toxic materials, and acidic gases to the mineral particles [*Huebert et al.*, 2003]. It was also found that a 24 hour-averaged clear-sky shortwave net radiative forcing ranges from -26 to -30 W m^{-2} over east Asian oceanic and coastal region [*Markowicz et al.*, 2003; *Bush and Valero*, 2003].

[5] These experiments were mostly done over oceanic areas far away from aerosol source regions and were limited on specific time periods. However, considering that the source regions for man-made aerosols are mainly situated over land areas, it must be important to examine the ARF near these source regions. Furthermore, the Asian continent is considered to be one of regions showing a variety of aerosols, including fossil fuel, biomass burning and dust aerosols, which suggest that the associated ARFs are highly region-dependent, due to the continental scale of emissions and the increase in fossil fuel consumption associated with the rapid economic growth [*Chameides et al.*, 1999].

[6] Despite the importance of the Asian continent as an aerosol source region there have been few measurements, especially in the desert area of north China. Moreover, due to the large spatiotemporal variations of aerosols, long-term monitoring near the source regions or their downwind areas is needed. Focusing on long-term monitoring of aerosols and an assessment of aerosol impact on the climate system over east Asia, a ground-based aerosol/radiation observation network, named the Skyradiometer Network (SKYNET), has been operating since 1997. Instruments used for observing surface solar radiation and aerosol characteristics include sky radiometer, pyranometer, and pyrheliometer. In addition, due to the interest in dust impact on the local and global climate, field experiments were conducted over east Asian seawaters, i.e., the Asian Atmospheric Particle Environmental Change Studies (APEX) [*Nakajima et al.*, 2003].

[7] In this paper, we will investigate the magnitude and varying degrees of aerosol influence on the solar radiation budget at the surface and TOA over east Asia using surface solar radiation measurements taken at SKYNET sites. Effort will also be made to interpret the relationship of these measurements to retrieved aerosol optical parameters. To this end, we developed a method of estimating ARF using retrieved aerosol optical parameters from sky radiometer measurements. In doing so, adjusted imaginary parts of refractive indices (and then single scattering albedos) estimated from the diffuse/direct method, originally introduced by *King and Herman* [1979] and extended by *Nakajima et al.* [1996b], were used as inputs into the exact radiative transfer (RT) model instead of using direct retrievals from sky radiometer measurements. In addition, special measurements taken during April in Korea and Japan were also analyzed in order to investigate the influences of Asian dust on radiative forcing downwind of east Asia.

2. Observation and Analysis

2.1. Surface Measurements of Solar Radiation

[8] Direct and diffuse solar radiation were measured using a sky radiometer (POM-01L, Prede Co. Ltd.) in daytime at seven wavelengths of 315, 400, 500, 675, 870, 940, and 1020 nm. Aerosol optical thickness, single-scattering albedo at five wavelengths (400, 500, 675, 870, and 1020 nm), Ångström exponent, and volume size distribution [$dV/d\ln r$ (cm^{3}cm^{-2})] were retrieved using an inversion software (i.e., SKYRAD.pack version 3) developed by *Nakajima et al.* [1996a]. A detailed explanation about quality control, retrieval methods, and sensitivity analysis can be found in the work of *Kim* [2003] and *Kim et al.* [2004].

[9] For the radiative forcing calculation, surface solar radiation measurements in the wavelength band between 0.3 and 4.0 μm were used in conjunction with aerosol optical properties obtained from the sky radiometer measurements. Direct solar fluxes were measured by the pyrheliometer, which measures the intensity of a radiant beam at normal incidence coming only from the solar disk with about 5 degrees of the full opening view angle. A shaded pyranometer was used to measure diffuse solar radiation, as both the pyranometer and the shading disk were mounted on an automated solar tracker to ensure that the pyranometer was continuously shaded. Then global downwelling solar fluxes were determined from direct solar radiation measured by pyrheliometer multiplied by the cosine of the solar zenith angle plus diffuse radiation by the shaded pyranometer. Although global downward solar fluxes were also measured by the pyranometer, the pyranometer tends to be more uncertain when the solar zenith angle is high because the detector responds differently to the solar incident angle [*Michalsky et al.*, 1995; *Satheesh et al.*, 1999]. Thus the global fluxes determined from both pyrheliometer and shaded pyranometer were preferable to those measured by the pyranometer.

[10] Measurements were taken at seven sites, given in Figure 1. Among them, four observation sites, i.e., Mandalgovi, Dunhuang, Yinchuan, and Sri-Samrong, form the SKYNET, while the Anmyon, Gosan sites of Korea, and the Amami-Oshima site of Japan are for the special radiation measurements made during the spring. The observation periods for the seven measurement sites are provided in Figure 2. Although measurement periods over the SKYNET observation sites appeared to be multiyears, the periods used for the radiative forcing calculations are limited and variable because of the mismatch between the sky radiometer and surface solar radiation measurements.

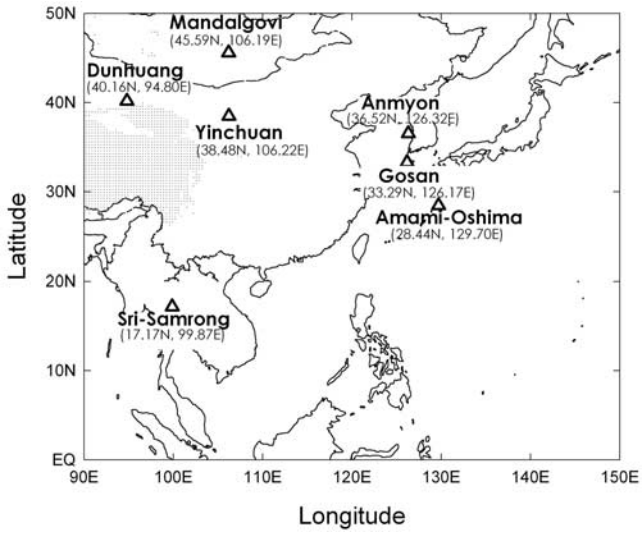

Figure 1. Geographical locations of observation sites.

Details of the geographical and climatological features of the observation sites can be found in the work of *Kim et al.* [2004].

2.2. Aerosol Optical Characteristics Over East Asia

[11] Optical properties of aerosols with seasonal and geographical variations over east Asia were investigated by sky radiation measurements at SKYNET sites. Measurements at Anmyon, Gosan in Korea and at Amami-Oshima in Japan during the Asian dust seasons were also analyzed for examining the optical properties of Asian dust particles. Although detailed descriptions are found in the work of *Kim et al.* [2004], it is worthwhile briefly summarizing the optical properties of aerosols over east Asia.

[12] Generally, aerosol optical thicknesses (AOTs) over east Asia were large compared with those found in North America or Europe, as there are various sources of aerosols, such as urban pollution, biomass burning aerosols, and dust particles. Also found are the significant temporal variations even for a given location; see the time series of optical properties at SKYNET sites provided in the work of *Kim et al.* [2004]. Moreover, most Chinese sites are found to be influenced by dusts, since dusts are transported from the arid/desert source regions in northern China and Mongolia to downwind areas.

[13] The largest size difference between fine and coarse modes shown in the volume size distribution for Mandalgovi was in coincidence with the largest variation of the Ångström exponent α (0.0–2.0), suggesting that various sizes of aerosols exist at Mandalgovi throughout the seasons. We applied a log-linear fit to optical thicknesses at five wavelengths for determining α. In Dunhuang, the fine mode as shown in Mandalgovi almost disappears throughout the year, and thus only the coarse mode exists, because Dunhuang is located at the eastern edge of the Takla Makan desert. The volume size distribution in Yinchuan shows a fine mode with a radius around 0.2 μm and a coarse mode with a radius around 5 μm, reflecting predominant urban-type aerosols in this area. The mode radius of fine mode at Sri-Samrong is around 0.2 μm, and the total volume of fine mode particles in volume distributions is largest among the sites, due to a predominance of biomass burning aerosols, especially during the winter, and we can also find signs of dust particles transported from the Indian arid region during April and May [*Sugimoto et al.*, 2002; T. F. Eck, personal communication, 2003]. The single scattering albedos (SSAs) of dust particles in Dunhuang, which is considered to be the source region, are around 0.91 at 0.5 μm with a standard deviation of 0.02 during the spring. Those values are greater than the previously known values of 0.63–0.89 [e.g., *Shettle and Fenn*, 1979; *Hess et al.*, 1998], but slightly smaller than around 0.93 of the Aerosol Robotic Network (AERONET) analysis for the Saharan dust [e.g., *Tanre et al.*, 2001; *Dubovik et al.*, 2002a] when AERONET values were converted to the SSA at 0.5 μm by applying a log-linear fit.

[14] Asian dusts found in Korean and Japanese areas appear to have quite different optical characteristics depending on sites, which in effect should be closely linked to different dust origins and mixing processes. The SSA tends to become smaller during the dust outbreak period, suggesting that industrial/urban aerosols transported from eastern China by the westerlies affect aerosol properties during the dust events through the mixing processes. Explaining such low SSAs during the dust events, two ways may be proposed. First, the strong winds accompanied with dust events simply transport more elementary carbons (EC) to the downwind sides. This conjecture seems consistent with observation that the EC amount was much increased during the dust event at Amami-Oshima [*Ohta et al.*, 2002]. Another plausible explanation is the mixing of dust particles with ECs, analogous to the analysis that dust particles from the North America were likely to be coated or aggregated with sulfate species and transported to the Bermuda area [*Anderson et al.*, 1996].

3. Methodology for Radiative Forcing Calculation

[15] For the radiative forcing calculation, we have developed an algorithm, adjusting aerosol parameters to bring in calculated values of diffuse and direct solar radiation close to observed values. Retrieval procedures used for the calculation of aerosol radiative forcing from ground-based

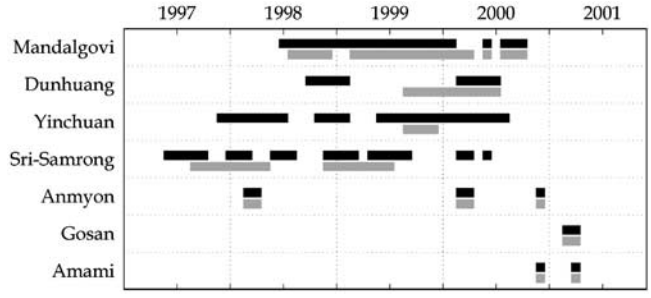

Figure 2. The observation periods covered by four SKYNET sites (Mandalgovi, Dunhuang, Yinchuan, and Sri-Samrong), and observation sites at Anmyon, Gosan, and Amami-Oshima. Black and gray solid lines represent the periods of sky radiometer observations and pyranometer/pyrheliometer observations, respectively.

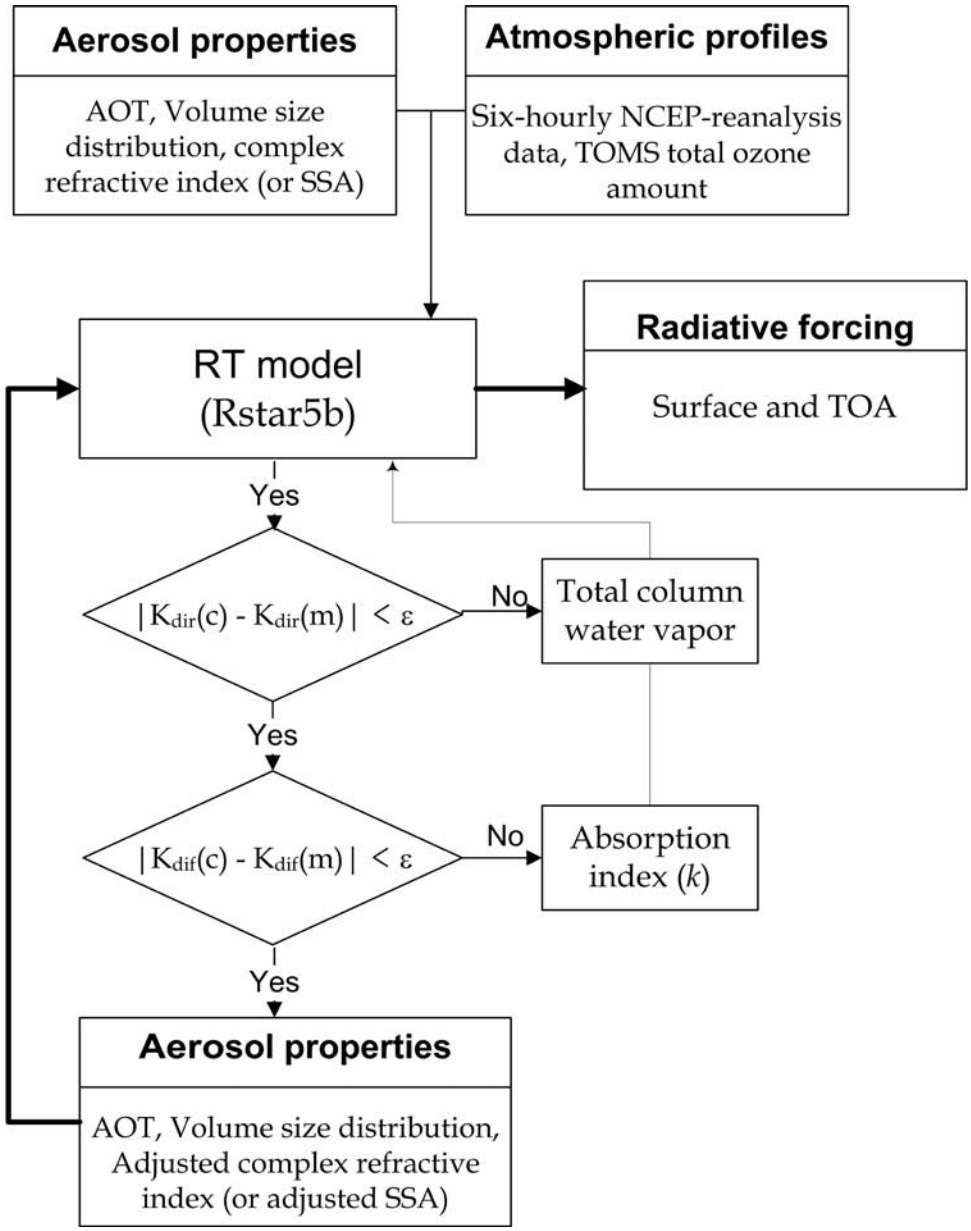

Figure 3. A schematic diagram for the procedures used in aerosol radiative forcing calculation from sky radiometer and surface solar flux measurements. K_{dir} and K_{dif} represent direct and diffuse fluxes, and *c* and *m* in parentheses represent calculated and measured values, respectively.

solar radiation measurements are provided in Figure 3. As illustrated at the top of Figure 3, aerosol optical parameters and atmospheric profiles are used as inputs into a RT model for simulating surface solar fluxes. For the flux calculation, we use the real part of refractive index retrieved from sky radiance measurements. Thus values vary with space and time, ranging from 1.45 to 1.70. During the retrieval, the columnar water vapor amount and the imaginary part of the refractive index (hereafter absorption index) are obtained by minimizing the difference between the calculated and measured fluxes, as suggested in the work of *King and Herman* [1979] and *Nakajima et al.* [1996b]. In doing so, the absolute accuracies of the pyrheliometer and pyranometer are used as the convergence criteria (ε) in Figure 3. The adjusted absorption index and columnar water vapor amount are then used for the forcing calculation.

3.1. Surface Solar Flux Simulation

[16] Surface solar radiative fluxes were calculated over the wavelength band from 0.3 to 4.0 μm using a RT model (rstar5b) developed by the Center for Climate System Research (CCSR), University of Tokyo, Japan. The RT model accounts for multiple scattering in the atmosphere by molecules and aerosol particles, and bidirectional surface reflection [*Nakajima and Tanaka*, 1986, 1988]. Gaseous absorptions were taken into account with an embedded Lowtran-7 absorption model [*Kneizys et al.*, 1988]. In this calculation, retrieved aerosol optical parameters, such as aerosol optical thickness, volume size distribution, and

Table 1. Monthly Mean Surface Albedo Used for the Flux Calculation at Observation Sites[a]

	MG	DH	YC	SS	AM	GS	AO
Jan.	0.67	0.26	0.21	0.18	0.08	0.08	0.07
Feb.	0.46	0.27	0.21	0.19	0.07	0.07	0.07
March	0.49	0.23	0.24	0.17	0.07	0.07	0.06
April	0.23	0.24	0.26	0.17	0.06	0.06	0.06
May	0.24	0.25	0.27	0.15	0.06	0.06	0.06
June	0.22	0.26	0.25	0.14	0.06	0.06	0.06
July	0.22	0.25	0.26	0.14	0.06	0.06	0.06
Aug.	0.20	0.24	0.23	0.13	0.06	0.06	0.06
Sept.	0.22	0.25	0.25	0.17	0.07	0.07	0.06
Oct.	0.21	0.22	0.22	0.16	0.07	0.07	0.07
Nov.	0.38	0.19	0.18	0.16	0.08	0.08	0.07
Dec.	0.53	0.25	0.19	0.18	0.08	0.08	0.07

[a]Abbreviations are as follows: Mandalgovi, MG; Dunhuang, DH; Yinchuan, YC; Sri-Samrong, SS; Anmyon, AM; Gosan, GS; and Amami-Oshima, AO.

complex refractive indices derived from sky radiation measurements at SKYNET sites, were used as inputs to the RT model. We assumed that the aerosol concentration was constant within a boundary layer of up to 3 km depth for the model. Such a constant concentration within the boundary layer is a generally accepted pattern, as noted in lidar experiments for aerosol profiles [*Takeuchi et al.*, 1999; *Sugimoto et al.*, 2002], and as also demonstrated in the work of *Liao and Seinfeld* [1998]. In the RT calculation, wavelength-dependent aerosol optical thicknesses are effectively used by providing the aerosol size distributions and a reference optical thickness at 0.5 μm. Six-hourly National Centers for Environmental Prediction (NCEP) reanalysis data were used for describing the atmospheric thermodynamic conditions, and total ozone amounts from the Total Ozone Mapping Spectrometer (TOMS) were used for calculating the ozone absorption. Specifying the surface albedo, we used the monthly mean ground albedo climatology (Table 1) obtained from the NASA Langley Research Center Atmospheric Sciences Data Center; see the Web site (http://eosweb.larc.nasa.gov/).

[17] Figure 4 shows the simulation results at Amami-Oshima under clear sky conditions. Before the use of measured surface fluxes, all data were smoothed using a 5-min averaging window. Clear sky cases were chosen; this means that if one measurement is outlying from the generally varying trend of the global flux, then that point is regarded as being cloud-contaminated and thus rejected. In addition, the criteria of 0.05 between two SSA sets which will be discussed in section 3.2 may help remove the possible thin cirrus contamination since the model calculation assumes clear sky condition while stable thin cirrus may pass the screening process only using sky radiometer or flux data. The mean slope and offset values between calculated and measured fluxes at Amami-Oshima are also given in Figure 4. The comparison shows that calculated and measured values are in good agreement with the correlation coefficients of 0.984, 0.945, and 0.994, for direct, diffuse, and global fluxes, respectively. However, calculated fluxes appear to be slightly underestimated in comparison to measured values, as noted in slopes of 0.99 and 0.94 for the direct and diffuse fluxes, respectively. The root mean square error (RMSE) between calculated and measured surface fluxes ranges from 15 W m^{-2} (about 7.3%) for the diffuse flux to 35 W m^{-2} (about 4.6%) for the direct flux. The discrepancies could be caused by errors in

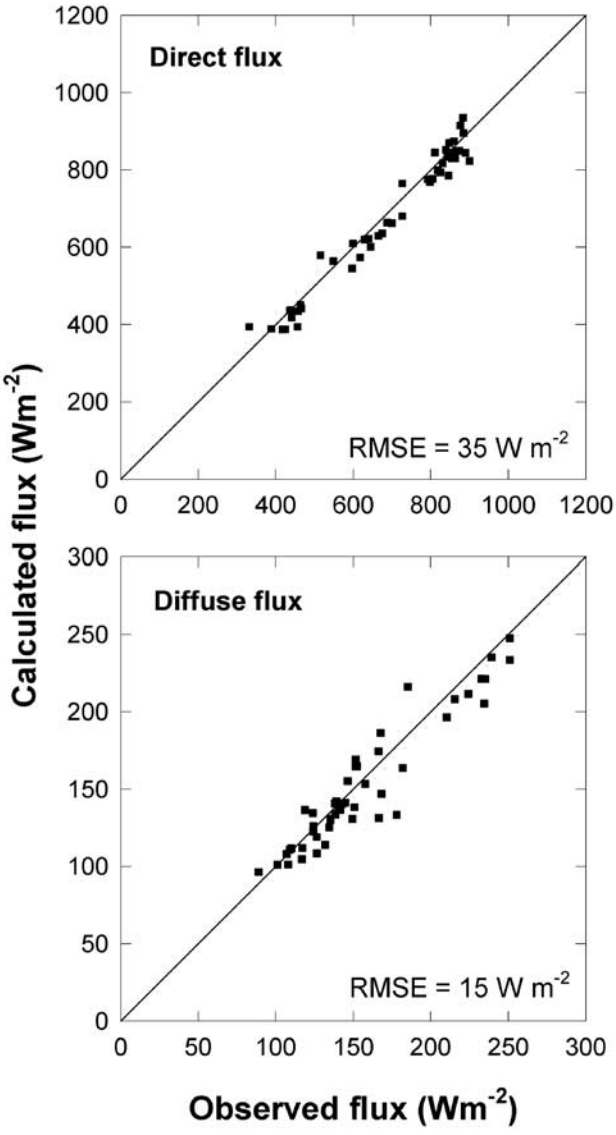

Figure 4. Scatterplots for the comparison of measured fluxes with calculated fluxes for the (top) direct and (bottom) diffuse solar fluxes.

the measured or assumed model input parameters, as well as errors in the flux measurements. Considering the absolute accuracy of the pyrheliometer and pyranometer are ±3 W m^{-2} and ±9 W m^{-2} [*Satheesh et al.*, 1999], respectively, the much larger RMS errors (15, and 35 W m^{-2}) noted in this simulation may be due to the more uncertain nature of the input parameters, in particular those associated with aerosols.

3.2. Single Scattering Albedo From the Diffuse/Direct Method

[18] Assuming the solar flux measurements are true and the radiative transfer modeling is accurate, the differences between calculated and measured fluxes may be due to inherent uncertainties in the input parameters (e.g., volume distribution, AOT, refractive index, surface albedo, and columnar water vapor amount). Among these input parameters, uncertainties induced by volume distribution and AOT appear to be minor as shown in Appendix A. We also point out that the largest uncertainties in flux simulation are from the SSA error. Thus, for any given surface albedo, differences between the calculated and measured solar fluxes would be mainly due to uncertainties in the absorption index and columnar water vapor amount.

[19] It has been shown that the absorption index and ground reflectivity can be estimated from the ratio between diffuse and direct solar fluxes, while the real part of the complex refractive index of aerosols is nearly independent of the diffuse/direct flux ratio [*King and Herman*, 1979]. These findings suggest that the absorption index (and then SSA) can be retrieved from the diffuse/direct flux ratio. By extending the method originally proposed by *King and Herman* [1979] that needs a range of solar zenith angle about 40° and nearly invariable aerosol properties during the narrowband flux measurements, *Nakajima et al.* [1996b] showed that the diffuse and direct solar radiative fluxes integrated over the whole solar radiation range can be used for simultaneously estimating the absorption index and columnar water vapor amount. Furthermore, from the sensitivity analysis of direct and diffuse fluxes to various input parameters they showed that the absorption index could be retrieved from the diffuse flux variations without specifically accounting influences from other parameters such as solar zenith angle and optical thickness.

[20] Applying the *Nakajima et al.* [1996b] approach, and assuming that discrepancies between calculated and measured solar radiation fluxes are mainly due to the uncertainties in the absorption index and columnar water vapor amount, we have adjusted the absorption index and columnar water vapor amount so that the model-simulated diffuse/direct fluxes are close to the measurements, as shown in Figure 3. In doing so, the absolute accuracies of the pyranometer and pyrheliometer are used as the convergence criteria for minimizing the differences between calculated and measured values of diffuse and direct fluxes.

[21] In order to examine the feasibility of using the diffuse/direct flux method for retrieving the absorption index and column water vapor amount, we simulated diffuse and direct fluxes with the varying columnar water vapor amount (i.e.: w = 1.0, 2.0, 4.0, and 8.0 g cm^{-2}), surface albedo (i.e.: R_s = 0.0, 0.1, 0.2, and 0.3), and absorption index (i.e.: k = 0.0, 0.005, 0.01, 0.025, and 0.05). In this study, the direct flux is defined as the flux measured by the pyrheliometer. The results are given in Figure 5. Each line in Figure 5 displays the flux changes with a respective varying parameter, while the other two parameters are held fixed. The chosen reference values at the crossing point are w = 2 g cm^{-2}, R_s = 0.1, and k = 0.01 in this case. In this simulation, a log-normal volume distribution with a fine (r_1 = 0.17 μm) and a coarse (r_2 = 3.44 μm) mode radius was assumed with a fixed Ångström exponent (α = 1.0), solar zenith angle (θ_0 = 60°), and aerosol optical thickness (AOT = 0.5). It should be noted that the surface direct flux variation is mainly due to the columnar water vapor amount whereas the diffuse flux variation is mainly controlled by the absorption index and surface albedo. Considering that the effect on diffuse flux changes with respect to albedo variation of 0.0–0.3 appear to be relatively smaller than the effect by absorption index variation of 0.0–0.05, the absorption index is the main component inducing uncertainties in the diffuse flux. For instance, surface albedo variation from 0.05 to 0.15 resulted in flux changes of less than about 5 percent. Detailed sensitivity results of retrievals to the various chosen parameters are given in the Appendix A1.

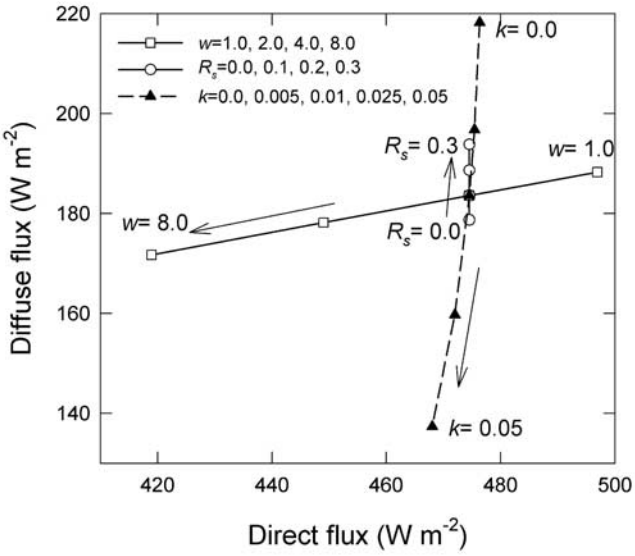

Figure 5. A schematic diagram showing the dependence of the direct and diffuse solar radiative fluxes on the surface albedo (R_s), columnar water vapor amount (w), and aerosol absorption index (k). Arrows represent incremental directions of respective parameters.

[22] The resultant columnar water vapor amount appears to be in good agreement with the radiosonde derived columnar water vapor amount (not shown). Moreover, the differences of columnar water vapor amount between retrievals from direct flux method and NCEP reanalysis data are very small, i.e., 0.12 g cm^{-2} of RMSE, suggesting that the flux method is sound.

[23] It should be mentioned that the refractive index is made invariant throughout the solar spectrum range, since only one averaged refractive index for all the channels is retrieved from the algorithm (i.e., skyrad.pack version 3).

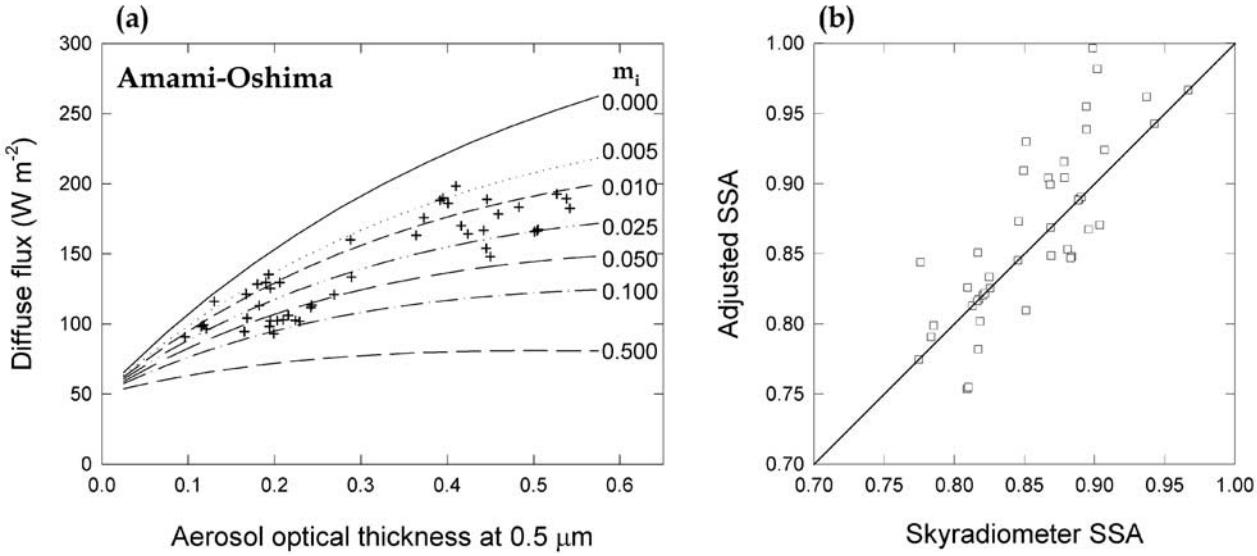

Figure 6. (a) Measured diffuse fluxes given with aerosol optical thickness at 0.5 μm. Theoretical diffuse fluxes calculated with various absorption indices (m_i) are embedded (curves). (b) Single scattering albedo (SSA) from sky radiometer measurements versus adjusted single scattering albedo at Amami-Oshima.

However, sensitivity tests for assessing the influence of fixed refractive indices on the diffuse radiation at the surface shows that only a few percent of diffuse flux change may be induced by the wavelength-independent assumption, although the changing magnitude seems to be increased with the increasing AOT; see Appendix A1. Thus we suggest that the effect of using the wavelength-independent refractive index seems to be minor. In contrast, the real part of refractive index retrieved from sky radiometer analysis is kept constant during the simulation.

[24] One example showing the retrieved absorption indices and associated SSAs is given in Figure 6. The measured diffuse fluxes given with 0.5 μm AOT at Amami-Oshima are overlaid with theoretical curves calculated with various absorption indices; see Figure 6a. For the simple demonstration, the results are given at the fixed solar zenith angle, i.e., $\theta_0 = 60°$. It should be noted that most of the retrieved absorption indices range from 0.005 to 0.1 at Amami-Oshima. Associated SSAs at 0.5 μm were obtained by using the method provided in Figure 3, with inputs of diffuse and direct solar fluxes, and aerosol parameters from the sky radiometer measurements. The resultant SSAs are compared against ones retrieved from the use of skyrad. pack; see Figure 6b. The bias and RMSE between two sets are 0.01 and 0.03, respectively. Although the bias remains small, the RMSE of 0.03 suggests that the correction of SSA can be significant in some cases.

[25] The advantage of this approach is that aerosol optical properties can be retrieved, at least being consistent with surface flux measurements. However, associated errors can be arisen from many different elements as indicated in Appendix A; therefore it is desirable to allow only a small adjustment while being cosistent with the measured surface radiation fluxes. For example, we suspect that the differences larger than 0.05 in particular for the cases of adjusted single scattering albedo greater than 0.9 are likely due to the cloud contamination. The sky with broken clouds or cirrus, which is discernable from the clear sky, may result in more scattered light but insignificant impact on direct solar radiation. Such cloud contamination can cause a smaller absorption index as shown in Figure 5. Because of this reasoning, retrieved SSA from the flux method was compared against one from sky radiation measurements only, and then the retrieval was discarded if the difference was greater than 0.05 for the calculation of aerosol radiative forcing.

[26] Also noted is that the algorithm used in this study is based on spherical particle assumption. However, for the accurate retrieval of aerosol properties from sky radiation measurements, it is important to consider the influences of nonspherical particles, especially of desert dust particles because retrieved results seem to show unrealistic spectral dependence in the real part of the refractive index and artificially increased fine particle mode [*Dubovik et al.*, 2000, 2002b]. The retrieved phase function also exhibits significant differences when spherical particles are assumed, but not to a degree to significantly alter single scattering albedo [*Dubovik et al.*, 2000, 2002b]. However, considering that the effects of dust nonsphericity are not significant in the retrieval of size distribution from *Nakajima et al.* [1996b], we suspect that those discrepancies may be due to the independent AERONET algorithm or invariant complex refractive index with wavelength used in this study. Nonetheless influences of nonsphericity are better to be incorporated for improving the retrieval qualities in particular for large dust particles.

[27] In addition, the absorption indices retrieved from both sky radiation and flux methods are an averaged value. Thus the retrieved SSAs cannot be directly compared against SSAs from AERONET measurements based on spectrally varying refractive indices. Note that SSAs retrieved in this study also vary with the wavelength because of the spectrally varying aerosol optical thickness. However, the uncertainty analysis in Appendix A shows that the mean differences of retrieved SSAs between from the variant indices and invariant assumption are within 0.015 although the differ-

ence tends to increase with the increased wavelength. Therefore the SSAs obtained from the fixed imaginary index in this study can be converted to the wavelength-dependent imaginary index within the 0.015 error margin.

3.3. Aerosol Radiative Forcing and Efficiency

[28] ARF is calculated by taking the difference in the net radiative flux between the case when aerosols are present and the case when aerosols are not present (i.e. zero aerosol), while holding the solar zenith angle, gaseous absorption, and atmospheric profiles invariant [*IPCC*, 2001]. As for the aerosol case, atmospheric conditions are prescribed with optical thickness, size distribution determined from sky radiation measurements, then fluxes are calculated to satisfy the surface boundary condition (i.e., downwelling surface flux) by adjusting the absorption index. Then, the 24-hour averaged ARF is obtained by taking an average of ARFs from all instantaneous measurements, based on the assumption that the aerosol optical properties measured at any given time are persistent throughout the day.

[29] Considering that changes in radiation energy within the Earth-atmosphere system are the ultimate forcing to induce climate change, understanding of how changes in aerosol optical properties can modulate ARF will lead to a better understanding of the climate system. To find how ARF depends on the aerosol parameters, we introduce the aerosol forcing efficiency ($\beta = \Delta_a F/\Delta\tau_{0.5}$) which is the rate of change of ARF ($\Delta_a F$) per unit AOT.

[30] At this point, it is quite interesting to examine how SSA and asymmetry factor (g) affect the aerosol forcing efficiency, because they are the two most important parameters controlling the forcing efficiency. We have done so by running the delta-Eddington two-stream method [*Meador and Weaver*, 1980] with varying SSA and g. We use the two-stream method because it can be used to easily determine the β change due to each varying parameter without computational burden. For testing the accuracy of simulated fluxes using the two-stream method, results are compared against ones from the exact calculation; see section A2. For a given observation site, varying ranges of SSA and g can be determined by adding (or subtracting) their one standard deviation. It is noted that one standard deviation of SSA ranging from 0.026 to 0.046 and g ranging from 0.020 to 0.057 can induce β changes as large as 80% and 20% at the surface, respectively, whereas 70% and 30% changes in β are induced by one standard deviation of SSA and g at the TOA, respectively. *Nakajima et al.* [2003] derived similar contribution ratios from their data analysis using a scaled optical thickness [$\tau^* = (1 - \omega_{0.5}(1 + g)/2)\,\tau_{0.5}$], in which $\omega_{0.5}$ and $\tau_{0.5}$ represent SSA and AOT at 0.5 μm, respectively. However, one standard deviation change of the second moment of the phase function makes a negligible impact on the surface β, and a difference of about 8% on the TOA β. The comparatively larger influence by the SSA change implies that the SSA is the most important parameter in determining aerosol influences on the radiation budget.

4. Results

[31] In this section, we present the results of retrieved ARFs from the flux method described in section 3. We first pay attention to Mandalgovi, Dunhuang, Yinchuan, and Sri-Samrong so that forcing characteristics associated with aerosol types can be discussed. In spite of three-year measurements over the SKYNET observation sites, retrievals are limited to particular periods (e.g., April–July at Dunhuang, September–December at Yinchuan, and December–March at Sri-Samrong) due to the mismatch between sky radiation data and surface solar fluxes, as shown in Figure 2. The radiative forcing efficiency for Asian dust, and the associated single scattering albedo and asymmetry factor will be discussed in the later part of this section, using the special measurements taken during April at Anmyon, Gosan, and Amami-Oshima.

4.1. ARF Over East Asia

[32] For an ARF calculation, simultaneous measurements of sky radiation and diffuse/direct solar radiation flux at the surface are required. Because of limited match-ups of sky radiation versus solar flux data due to the inhomogeneous data coverage, the ARF coverage is also limited. Therefore ARF is given with the number of match-ups used for the forcing calculation in each month; see the left panels of Figure 7. The middle panels of Figure 7 display the 24-hour averaged surface ARFs (W m^{-2}) given with AOT at 0.5 μm at Dunhuang, Yinchuan, and Sri-Samrong. The match-ups available for Mandalgovi were not enough to represent aerosol forcing characteristics in that area, so that results obtained from measurements for Mandalgovi are not presented.

[33] The relatively small number of available data for each month was largely due to the cloud contamination. However, it was also contributed by the employed assumption that the SSA from sky radiation measurents should be consistent with the adjusted SSA, allowing only a small adjustment to satisfy the measured surface radiation fluxes. The retrieved SSA from the flux method was compared against the one from sky radiation measurements only, and then the retrieval was discarded if the difference was greater than 0.05. In Figure 7, calculated ARFs (represented by cross hairs) are given as a function of optical thickness at 0.5 μm. Also provided are theoretically calculated SSAs (represented by curves) at 0.5 μm, which range from 1.0 (top curve) to 0.6 (bottom curve) with a 0.05 interval. For the simpler demonstration using the reduced number of parameters, theoretical SSAs at each site were calculated using mean values of aerosol volume size distribution and surface albedo, but with varied optical thickness. Because of this, some points appear to have unrealistic SSAs greater than unity. Also given in the middle panels of Figure 7 are the mean SSA and g. In addition, mean β at the TOA, atmosphere, and surface are provided in the right panels of Figure 7.

[34] As described in section 2.2 Dunhuang is influenced mainly by dust particles all year around. In Yinchuan, the general aerosol characteristics are related to the accumulation processes of urban aerosols throughout the year, and dusts during the springtime. Sri-Samrong showed patterns for biomass burning aerosols during mid-October to mid-February. The results obtained in this study over those three sites will be interpreted with the aid of typical aerosol types found at those observation sites. Details of aerosol characterization and their seasonal variations

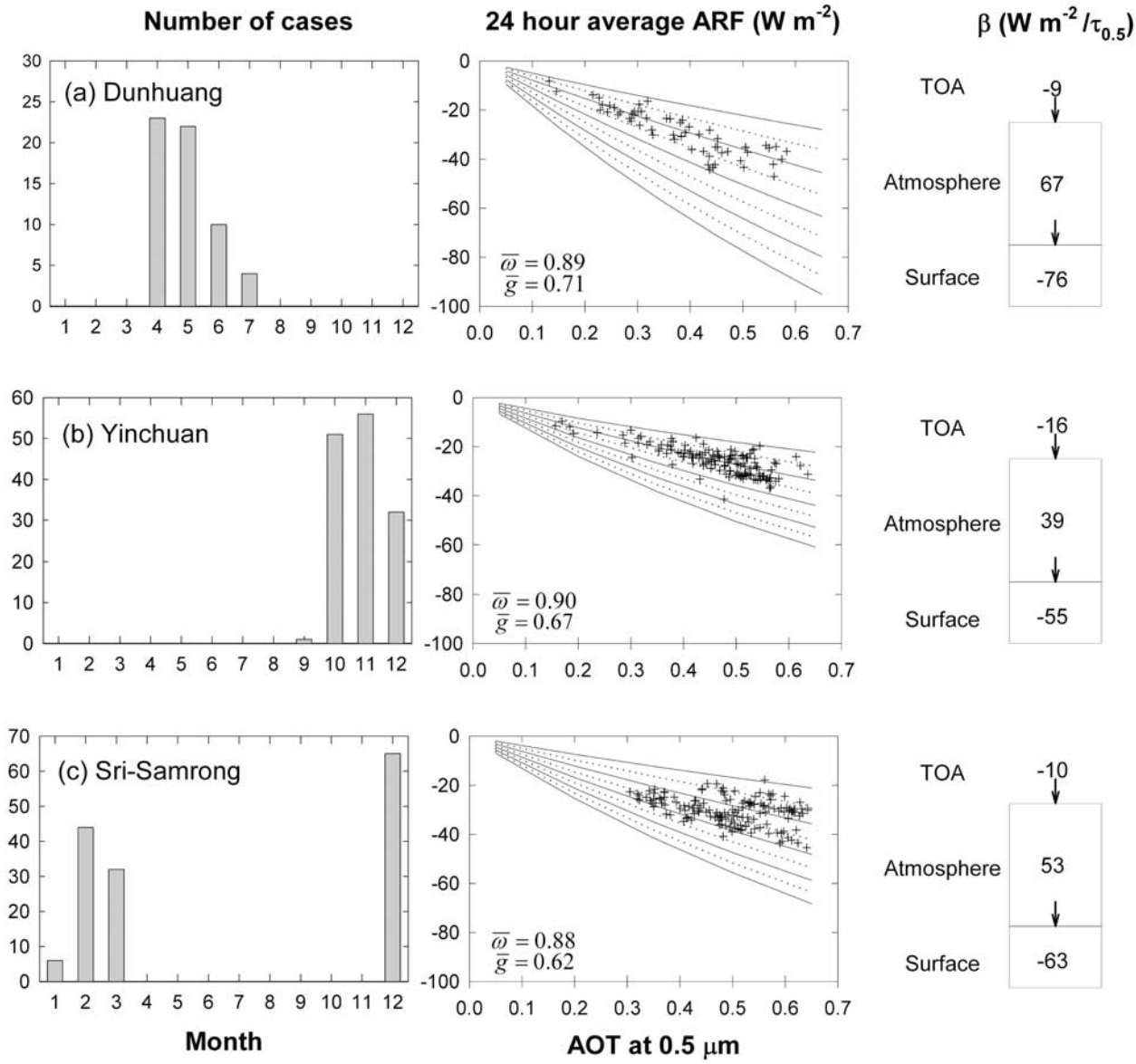

Figure 7. Number of cases used in each month, 24-hour averaged surface radiative forcing (W m^{-2}) with AOT at 0.5 μm, and forcing efficiency (β) given in W m^{-2} at (a) Dunhuang, (b) Yinchuan, and (c) Sri-Samrong. Curves represent the theoretical radiative forcing calculated with SSAs of 1.0 (top curve) to 0.6 (bottom curve), with a 0.05 interval. Cross hairs represent observed forcing. Here $\overline{\omega}$ and $\overline{g}$ represent mean single scattering albedo and asymmetry factor at 0.5 μm, respectively.

for those sites are found in the work of *Kim et al.* [2004].

[35] Because Dunhuang is largely affected by frequent Asian dust episodes during the spring to early summer period, ARFs for Dunhuang found in this study are largely due to Asian dust aerosols. The mean SSA and g are 0.89 and 0.71, respectively. The SSA obtained in this study at 0.5 μm is slightly smaller than 0.92∼0.93 at 0.44 μm found over the Saharan desert or Saudi Arabia [*Dubovik et al.*, 2002a], implying that Asian dusts are more absorbing aerosol. However, the obtained g (≈0.71) is close to the values found in the Saharan desert (≈0.72) or Saudi Arabia desert (≈0.68) [*Dubovik et al.*, 2002a].

[36] The resultant forcing efficiency in the atmosphere is about 67 W m^{-2}, suggesting that Asian dusts over the Dunhuang area absorb a significant amount of solar radiation. Combining with the relatively smaller forcing efficiency at the TOA (≈−9 W m^{-2}), the overall surface forcing efficiency is estimated to be −76 W m^{-2}, indicating that the surface is deprived of a substantial amount of solar energy in the presence of Asian dusts. The smaller TOA forcing efficiency seems to be associated with high surface reflectivity over the Dunhuang area, since the negative TOA forcing can be reduced by the aerosol absorption of surface-reflected upwelling radiation, in particular under high surface albedo conditions, as noted in Sahara dust studies [*Haywood et al.*, 2001, 2003; *Myhre et al.*, 2003]. More

discussion on the influences of Asian dusts on the ARF is found in section 4.2.

[37] Yinchuan represents the urban type aerosol because the match-up data only cover the September–December period. The obtained SSA of around 0.9 is similar to the SSA (0.87 to 0.90) found over the Indian Ocean during the INDOEX period [*Satheesh and Ramanathan*, 2000]. However, 0.9 of SSA in Yinchuan is much smaller than 0.98 at 0.44 μm for urban type aerosols observed at the NASA Goddard Space Flight Center (GSFC) [*Dubovik et al.*, 2002a]. This variability of SSA for urban type aerosols may be due to differences in fuel types and emission conditions. Automobile traffic should be the main local source of the pollution around the GSFC. However, the highly absorbing optical properties in the INDOEX are mainly due to the presence of soot type aerosols from inefficient fossil fuel combustion for heating and cooking, and biomass burning [*Satheesh et al.*, 1999]. Considering that aerosols from inefficient fossil fuel combustion are also abundant over China [*Chameides et al.*, 1999], we suspect that the small SSA value in Yinchuan is also due to the contributions of soot type aerosols to SSA.

[38] The period from December to March corresponds to the dry winter season over the Sri-Samrong area, and thus the prevailing aerosol type is the biomass burning [*Kim et al.*, 2004]. The retrieved SSA (≈0.88) representing biomass burning aerosols over the Sri-Samrong area is slightly larger than the 0.85 for African Savanna smoke but smaller than the 0.93 for the smoke over Amazonian forested regions [*Eck et al.*, 1998, 2001; *Dubovik et al.*, 2002a]. There are two bundles of points separated by about 0.9 line of SSA; one showing the mean SSA around 0.91 during December 1998 and the other showing a smaller mean SSA around 0.86 during January to March in 1998. Since both groups show a positive relationship between AOT and α (not shown) which is common for biomass burning aerosols, the different SSAs suggest that aerosol origin and composition during December are different from those for the January–March period, i.e., there are more absorbing aerosols during the latter period.

4.2. ARF for Asian Dusts During April

[39] Satellite-based retrievals and model simulations of aerosols show features of aerosol outflow from the continent to the open sea near Korea and Japan under prevailing westerly conditions [*Haywood et al.*, 1999; *Higurashi et al.*, 2000; *Higurashi and Nakajima*, 2002; *Takemura et al.*, 2002]. Especially, a large amount of Asian dust is uplifted in northern China and transported to a wide oceanic region in the east during the spring. A significant increase in dust particles over east Asia and adjacent Pacific regions in spring must alter the radiation balance over those regions because of dust-radiation interactions. Thus it is a natural question to ask about the extent to which radiation energy is altered by the presence of Asian dusts. In order to study the impact of Asian dust on the radiation budget, we calculated the forcing efficiency at Anmyon and Gosan of Korea, and at Amami-Oshima of Japan during April, in which dust episodes are often observed. Since all sites are located on the western side of the islands, they should have been less affected by locally produced aerosols under the westerly conditions. Therefore these sites are suitable for examining the influence of aerosols originated from China on radiative forcing.

[40] Figure 8 shows the 24-hour averaged ARF given with AOT and the associated forcing efficiency for Anmyon during April 2000, and for Gosan and Amami-Oshima during April 2001. In order to examine dust influences, we separated the observation data into nondust cases or Asian dust cases using the criteria given in the work of *Kim et al.* [2004].

[41] It was shown that the nondust cases in Anmyon are mainly influenced by urban type aerosols during April [*Kim et al.*, 2004]. The obtained SSA of around 0.87 at Anmyon is smaller than the 0.9 found in Yinchuan, but similar to the SSA from the INDOEX. The highly absorbing aerosols in Anmyon may be explained by the environmental conditions of the surroundings: urban-type aerosols are emitted by a power plant located northwest 40 km away from the site and seem to be transported into the site area. It is known locally that the CO_2 concentration at Anmyon is highly correlated with the operational status of the power plant, i.e., there is a significantly increased CO_2 concentration during the operation period (personal communication with local observers in the Anmyon GAW Observatory), implying that the lower SSA is likely to be associated with fossil fuel combustion at the power plant.

[42] The AOT versus α relationships for Gosan and Amami-Oshima exhibit a general negative relationship between α and AOT, and the varying degree of AOT and α appear to be similar to each other [*Kim et al.*, 2004]. However, the 0.92 of SSA in Gosan is larger than the 0.86 in Amami-Oshima during April. Since Amami-Oshima is located far south in the open ocean, there should not be any local sources for the urban type aerosols that can bring about a lower SSA. Therefore the only explanation for the lower SSA found in Amami-Oshima should be the air mass transport from a region where rich in elementary carbon. Considering the fact that Amami-Oshima is located further south than Gosan, Amami-Oshima has simply more chances than Gosan has to encounter a polluted air mass if there is a northwesterly wind than Gosan has. For example, when there is a northwesterly flow passing through the Shanghai area, urban aerosols can arrive in Amami-Oshima while keeping away from the Gosan area. In fact, trajectory analysis indicated that the high concentration of aerosol in Amami-Oshima is closely related to a northwesterly that can transport a polluted air mass from the inland northeast China and the industrial/urban area on the east coast of China [*Tsuruta et al.*, 2003]. Supporting this notion, Amami-Oshima experienced high concentrations of elemental carbons (EC) under the northwesterly conditions during the period of 11–16 April [*Ohta et al.*, 2002; *Tsuruta et al.*, 2003], in contrast to the slightly increased EC concentrations in Gosan [*Chuang et al.*, 2003]. In contrast to the quite different SSAs, nearly equal asymmetry factors (≈0.69) are found in the three sites, suggesting that the aerosol size distribution of the nondust cases is similar to each other during April.

[43] Results for dust cases are given in the right panels of Figure 8. The magnitudes of SSA (0.80–0.86) at the three sites during Asian dust events appear to be smaller than the 0.9 found in Dunhuang during spring. The lower SSA is likely to be due to the extensive mixing of dust particles with EC over China during the dust movement, as studied in

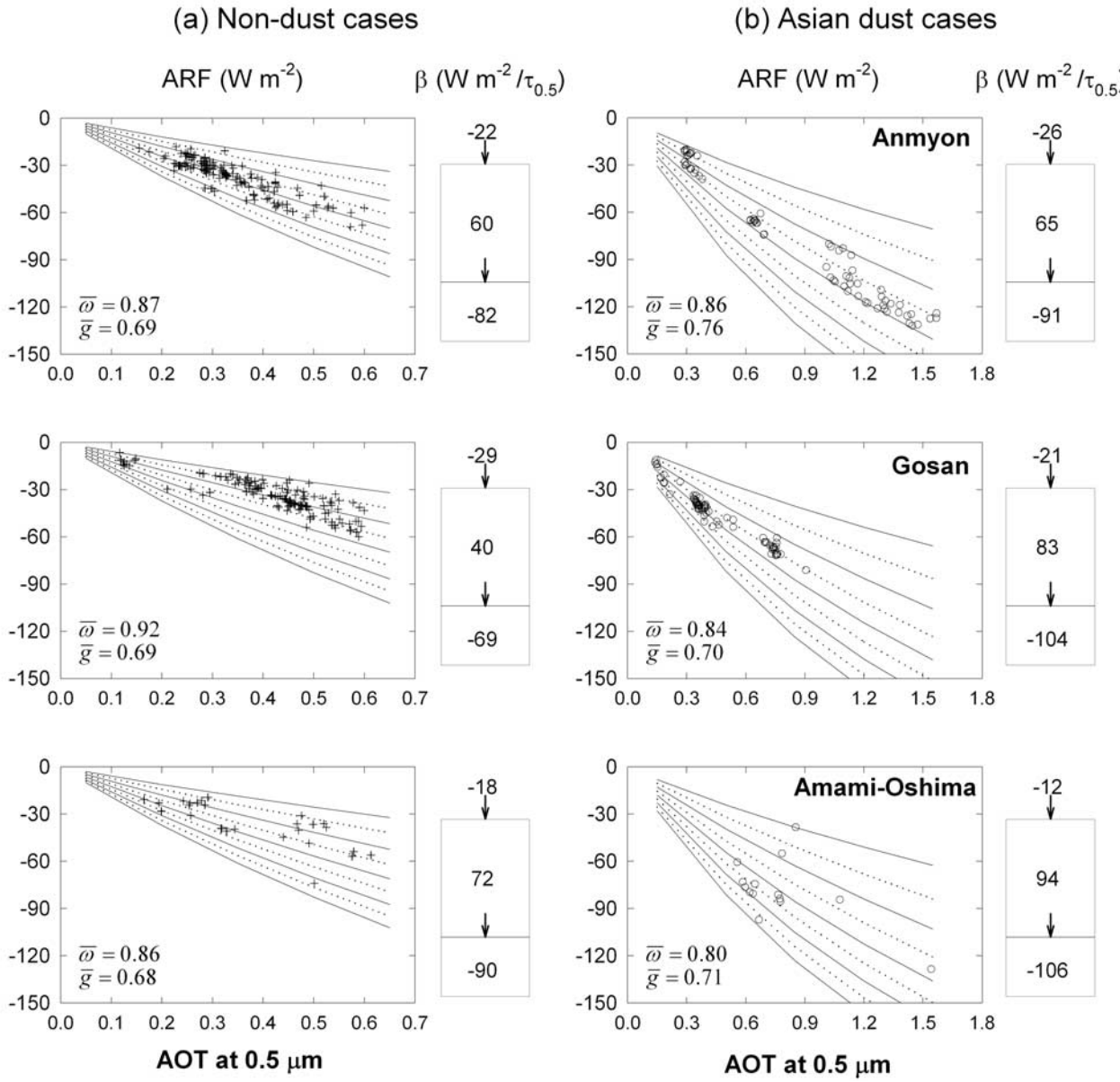

Figure 8. The 24-hour averaged surface radiative forcing (W m^{-2}) with AOT at 0.5 μm and forcing efficiency β (W m^{-2}) at Anmyon, Gosan, and Amami-Oshima for (a) nondust cases and (b) Asian dust cases. Curves represent the theoretical radiative forcing calculated with SSAs of 1.0 (top curve) to 0.6 (bottom curve), with a 0.05 interval. Here $\bar{\omega}$ and $\bar{g}$ represent mean single scattering albedo and asymmetry factor at 0.5 μm, respectively.

the work of *Tsuruta et al.* [2003]. *Ohta et al.* [2002] showed that the EC fraction was increased by fine particles at Amami-Oshima during dust events. Consistent with their results, the lower SSA at Gosan was mainly due to submicron particles [*Andrews et al.*, 2001].

[44] Since the mixing of fine dust particles with EC aerosols requires time to interact while moving through the industrial/urban area, the dust moving speed and its path seem to be critical elements for determining the SSA in the downwind side. In general, coarse particles are abundant in the dusts observed in Anmyon during April 2000, due to the fast moving dust storm, resulting in comparatively higher SSA (≈0.86) and thus lower atmospheric absorption, around 65 W m^{-2}.

[45] However, Gosan and Amami-Oshima seemed to experience slowly moving dust storms, which allow the fine particles more time to coagulate with EC. Lower SSA value (and thus larger atmospheric absorption) at Amami-Oshima may be related to the path of the dust storm. For example, trajectory analysis indicated that dusts that arrived in Amami-Oshima originated from western Mongolia and passed through the industrial/urban Shanghai area, while the air mass that arrived at Gosan on 12 April took a path from the eastern part of Mongolia through the Bohai bay. Because of this, the SSA at Amami-Oshima (≈0.80) is smaller than at Gosan (≈0.84). Accordingly the atmospheric forcing efficiency (≈94 W m^{-2}) is largest in Amami-Oshima due to the lowest SSA.

[46] The g (0.70–0.71) obtained at Gosan and Amami-Oshima are consistent with the values found in Dunhuang (≈0.71), Saharan desert (≈0.72) or Saudi Arabian desert (≈0.68). However, 0.76 of g at Anmyon is larger than from other different regions. This may be due to the exceptionally coarse particles found on the 7 April 2000 dust event, which caused most of public schools to shut down in Korea.

[47] Overall, the dust forcing efficiency in the atmosphere, of 65–94 W m^{-2}, over Korea and Japan suggests that Asian dusts absorb a significant amount of solar radiation. Combined with the strong cooling effect on the surface, the Asian dust seems to have an impact on increasing atmospheric stability.

5. Summary and Conclusions

[48] In order to characterize the aerosol optical properties and associated radiative forcing in east Asia, we developed a method to calculate the ARF utilizing analyzed aerosol optical parameters from sky radiometer measurements and surface solar fluxes at the SKYNET observation sites (here Mandalgovi, Dunhuang, Yinchuan, and Sri-Samrong), and at three special sites (Anmyon, Gosan, and Amami-Oshima). In doing so, the calculation of diffuse solar fluxes is iterated until it matches with the measured surface flux (i.e., surface boundary conditions) by adjusting the absorption index. The basic idea of conducting such an iteration process is that the difference between the calculated and the measured surface diffuse fluxes is mainly due to the uncertain absorption index. In other words, other optical input parameters such as optical thickness and size distribution are retrieved with a fair accuracy from the sky radiation measurements.

[49] In Dunhuang, in which Asian dusts are the predominant aerosols, the mean SSA and g are 0.89 and 0.71, respectively. The forcing efficiency in the atmosphere is about 67 W m^{-2}, suggesting that Asian dusts over the Dunhuang area absorb a significant amount of solar radiation.

[50] Yinchuan, in which urban aerosols are dominant during the September–December period, shows an SSA of around 0.9, which is similar to the SSA found over the Indian Ocean during the INDOEX period, but much smaller than the urban type aerosols observed in NASA/GSFC. Considering that aerosols from the inefficient combustion of fossil fuels are also abundant over China, we suspect that the small SSA value in Yinchuan is contributed by soot type aerosols such as seen in the INDOEX region.

[51] In the Sri-Samrong area, where biomass burning aerosols are prevalent during the winter period, the obtained SSA is about 0.88; that is slightly larger than the 0.85 for African Savanna smoke but smaller than the 0.93 for the smoke over the Amazonian forested regions. Interestingly, there seems to be two groups of biomass burning aerosols, depending on the analysis period, i.e., December period and January–March period, whose respective SSAs are 0.91 and 0.86. These findings may lead to a conjecture that the Sri-Samrong area is progressively influenced by more absorbing biomass burning aerosols, perhaps from different origins and with different composition, over the time during the winter dry season.

[52] As an important conclusion, it can be pointed out that aerosols in east Asia tend to have a smaller single scattering albedo compared to the same type of aerosols found in other areas, and thus the atmosphere tends to absorb more solar radiation.

[53] From the analysis of sky radiation and surface flux measurements taken during April at Anmyon, Gosan in Korea, and Amami-Oshima in Japan, with an emphasis on the dust influence on the radiation budget, it was found that the SSAs of Asian dusts are smaller, compared to the ones in the source region. The SSA of 0.89 found in Dunhuang is significantly larger than the 0.86, 0.84, and 0.80 found in Anmyon, Gosan, and Amami-Oshima, respectively. Since the dust particles uplifted in the arid/desert region of northern China and Mongolia move through the industrial/urban area located in East China where EC aerosols are abundant, the one way to explain the decreased SSA in the downwind area may be the mixing processes noted in the work of *Chuang et al.* [2003]. Although the dust effect on the forcing efficiency is highly variable from location to location, it is clear that the Asian dust, blackened during its movement, absorbs more solar energy than it does at the origin.

Table A1. Retrieval Errors of Aerosol Optical Thickness [$\tau_a(\lambda)$], Size Distribution [$dV/d\ln r$ (r_i)], and Single Scattering Albedo [w_0 (λ)] Under the Different Optical Thickness and Solar Zenith Angle Conditions[a]

Condition	$\theta_0 = 30$	$\theta_0 = 60$
	$\tau_a(\lambda)$	
τ_a (0.5 μm) = 0.2	0.02 (0.01)	0.00 (0.01)
τ_a (0.5 μm) = 0.5	0.01 (0.01)	0.01 (0.01)
τ_a (0.5 μm) = 1.0	−(0.06)	-
	$dV/dlnr$ (r_i)	
0.1 μm < r < 10 μm	8% (10%)	6% (18%)
r < 0.1 μm and r >10 μm	8–100% (10–100%)	6–100% (18–100%)
	m_r	
τ_a (0.5 μm) ≤ 0.5	0.0 (0.0)	0.0 (0.0)
τ_a (0.5 μm) = 1.0	−(0.1)	-
	m_i	
τ_a (0.5 μm) ≤ 0.5	0.0% (0.0%)	0.0% (0.0%)
τ_a (0.5 μm) = 1.0	−(100%)	-
	w_0 (λ)	
τ_a (0.5 μm) = 0.2	0.08 (0.01)	0.01 (0.01)
τ_a (0.5 μm) = 0.5	0.01 (0.01)	0.01 (0.01)
τ_a (0.5 μm) = 1.0	−(0.07)	-

[a]Errors for dust particles are given in parentheses. Errors in the retrieved size distribution and m_i are given in percent.

Appendix A

A1. Uncertainty Test

A1.1. Retrievals of Aerosol Optical Properties From Sky Radiation Measurements

[54] In order to assess the performance of algorithm for retrieving aerosol optical properties from sky radiation measurements, we first simulated sky radiation under the conditions of $\tilde{m} = 1.5–0.01i$, $r_{min} = 0.01$ μm, $r_{max} = 20$ μm, surface albedo = 0.1, and with four different aerosol optical thicknesses at 0.5 μm (i.e., $\tau_a = 0.05$, 0.2, 0.5, and 1.0), and with two solar zenith angles (i.e., $\theta_o = 30°$, and 60°). For the dust particle, $\tilde{m} = 1.55–0.005i$ was used. In this simulation,

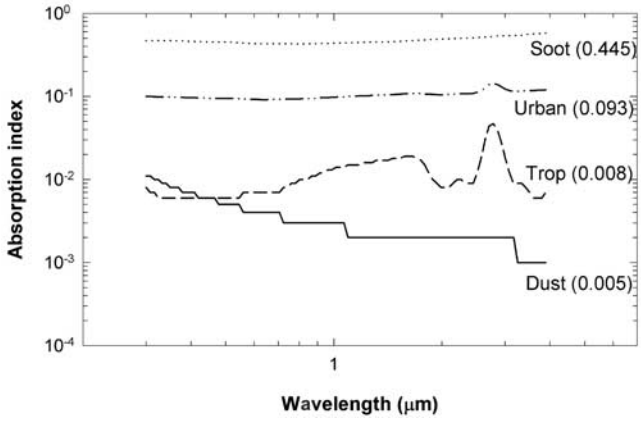

Figure A1. Imaginary parts of the refractive indices for the soot, urban, tropospheric, and dust type aerosols [*Shettle and Fenn*, 1979]. The values in the parentheses represent mean imaginary indices over the wavelength.

a log-normal volume distribution with a fine mode (r_1 = 0.17 μm) and a coarse mode (r_2 = 3.44 μm) was assumed. For the volume size distribution for the dust, the volume ratio of the coarse mode particle was set ten times larger than the fine mode particle. Then aerosol optical properties such as aerosol optical thickness, volume distribution, complex refractive index, and single scattering albedo were retrieved from the simulated sky radiation.

[55] Table A1 shows estimated errors of the retrieved aerosol optical thickness [$\tau_a(\lambda)$], size distribution [$dV/dlnr$ (r_i)], real and imaginary refractive index [$\tilde{m} = m_r - im_i$], and single scattering albedo [w_o (λ)]. Errors of the dust particles are presented in parentheses, and retrieval errors of optical properties with large optical thickness of 1.0 and solar zenith angle of 60° are not presented due to the failure of convergence in the retrieval process.

[56] As for the retrieval of aerosol optical thickness, the accuracy appears to be high although the uncertainty tends to be larger if solar zenith angle and optical thickness become smaller. The retrieval of refractive index under the aerosol optical thickness smaller than 0.5 shows high accuracy, although uncertainties become larger for dust particles when optical thickness is 1.0. The retrieval errors of particle size distributions are less than 8% when particle radius is between 0.1 and 10 μm, however, errors tend to be substantially large when radius is off those two boundaries. Thus it may suffice to say that size distributions can be retrieved with a relatively high accuracy within the radius range between 0.1 and 10 μm.

[57] Although uncertainties in retrieved single scattering albedo become larger when optical thickness is thinner and solar zenith angle is smaller, the sensitivity test shows that the single scattering albedo can be retrieved with a reasonably high accuracy. The accuracy of dust optical thickness and single scattering albedo appears high when aerosol optical thickness is less than 0.5, but the retrieval errors become larger around 0.06 and 0.07, respectively when optical thickness is large around 1.0. The uncertainty test of size distributions for dusts shows that errors reach 18% when the radius is between 0.1 and 10 μm. And the retrieval errors of real and imaginary part of refractive index also show errors about 0.1 and 100%, respectively, when the optical thickness is 1.0. The error analysis for dust particles shows that the overall retrieval errors in optical properties for dusts appear to be larger under optically thick conditions.

A1.2. Uncertainties in Surface Solar Flux and ARF

[58] In this study, SSA and aerosol radiative forcing were estimated using spectrally invariant imaginary part of the refractive index and monthly mean surface albedos independent of the solar zenith angle as inputs to the RT model. Thus it is worthwhile to conduct the sensitivity test of examining how those assumptions may affect simulated surface solar flux and thus aerosol radiative forcing.

[59] In order to assess the accuracy of radiative transfer calculations due to such assumptions, we first simulated diffuse and direct fluxes under conditions of aerosol optical thickness at 0.5 μm ($\tau_{0.5}$ = 0.2, 0.5), surface albedo ($\overline{A}$ = 0.1), and solar zenith angle (θ_o = 60°). Influences of the use of spectrally independent imaginary part of refractive index are examined by comparing results obtained from the use of

Table A2a. Spectral Independence of Imaginary Index (Albedo = 0.1): Error Analysis for Direct, Diffuse Flux (W m^{-2}), and Single Scattering Albedo Induced by Spectrally Invariant Absorption Index ($\overline{m}_i$), and Errors in Surface Albedo (A = 0.4 With a 0.1 Error Range) at AOT = 0.2 and 0.5[a]

	Direct Flux			Diffuse Flux			Single Scattering Albedo		
AOT	m_i (λ)	$\overline{m}_i$	ΔF, %	m_i (λ)	$\overline{m}_i$	ΔF, %	m_i (λ)	$\overline{m}_i$	$\Delta\omega_0$, %
					Soot				
0.2	743.1	740.6	2.5 (0.3)	41.1	41.2	0.1 (0.2)	0.235	0.237	0.002 (0.8)
0.5	527.6	523.3	4.3 (0.8)	34.5	34.5	0.0 (0.0)	0.235	0.237	0.002 (0.8)
					Urban				
0.2	731.6	731.4	0.2 (0.0)	87.6	86.5	1.1 (1.3)	0.651	0.640	0.011 (1.7)
0.5	505.4	505.2	0.2 (0.0)	115.0	112.8	2.2 (2.0)	0.651	0.640	0.011 (1.7)
					Troposphere				
0.2	752.4	753.3	0.9 (0.1)	117.0	116.3	0.7 (0.6)	0.965	0.952	0.013 (1.4)
0.5	547.3	549.3	2.0 (0.4)	179.2	177.9	1.3 (0.8)	0.965	0.952	0.013 (1.4)
					Dust				
0.2	682.2	682.0	0.2 (0.0)	141.1	139.5	1.6 (1.2)	0.892	0.893	0.001 (0.1)
0.5	416.6	416.4	0.2 (0.0)	218.4	214.2	4.2 (2.0)	0.892	0.893	0.001 (0.1)

[a]Four types of aerosols (soot, urban, tropospheric, and Asian dust particles) are considered. ΔF and $\Delta\omega_0$ represent flux and single scattering albedo changes, respectively. The percentage changes are given in parentheses.

Table A2b. Albedo Uncertainty (Error = 0.1): Error Analysis for Direct, Diffuse Flux (W m^{-2}), and Single Scattering Albedo Induced by Spectrally Invariant Absorption Index ($\overline{m}_i$), and Errors in Surface Albedo (A = 0.4 With a 0.1 Error Range) at AOT = 0.2 and 0.5[a]

	Direct Flux		Diffuse Flux		Single Scattering Albedo	
AOT	A = 0.4	ΔF, %	A = 0.4	ΔF, %	A = 0.4	$\Delta\omega_0$, %
			Soot			
0.2	740.6	0.0 (0.0)	46.3	1.7 (3.7)	0.237	0.0 (0.0)
0.5	523.3	0.0 (0.0)	37.1	0.9 (2.3)	0.237	0.0 (0.0)
			Urban			
0.2	731.4	0.0 (0.0)	95.8	3.2 (3.3)	0.640	0.0 (0.0)
0.5	505.2	0.0 (0.0)	120.4	2.6 (2.2)	0.640	0.0 (0.0)
			Troposphere			
0.2	753.3	0.0 (0.0)	131.4	5.2 (4.0)	0.952	0.0 (0.0)
0.5	549.3	0.0 (0.0)	196.6	6.5 (3.4)	0.952	0.0 (0.0)
			Dust			
0.2	682.0	0.0 (0.0)	154.3	5.1 (3.3)	0.893	0.0 (0.0)
0.5	416.4	0.0 (0.0)	231.6	6.0 (2.6)	0.893	0.0 (0.0)

[a]Four types of aerosols (soot, urban, tropospheric, and Asian dust particles) are considered. ΔF and $\Delta\omega_0$ represent flux and single scattering albedo changes, respectively. The percentage changes are given in parentheses.

spectrally varying $m_i(\lambda)$ for four aerosol types by *Shettle and Fenn* [1979], i.e., soot, urban, tropospheric, and dust type aerosols, whose imaginary part of refractive indices are given in Figure A1.

[60] Sensitivity results from the spectrally independent imaginary indices to the use of Shettle and Fenn's spectrally varying indices are presented in Tables A2a and A2b in terms of flux differences (W m^{-2}) and percent errors (%) for diffuse flux, direct flux, and single scattering albedo. It is shown that results from the use of spectrally independent imaginary index are not significantly different from those from spectrally varying imaginary indices although differences as large as 4 W m^{-2} (about 2%) are found in the dust case when AOT is 0.5. Overall it appears that the errors of single scattering albedo from using spectrally independent imaginary index are within 0.015 for all aerosol models.

[61] To assess the uncertainties in calculated direct/diffuse fluxes associated with errors in surface albedo, we tested simulation results for the given surface albedos varying from 0.05 to 0.40 with a 0.05 interval. Since the range of surface albedo in Table 1 is from 0.06 to 0.67, we present the results from surface albedo of 0.4 with a 0.1 error range. Diffuse flux changes caused by 0.1 of surface albedo error show larger differences around 3–4% under lower AOT about 0.2 than those around 2–3% under higher AOT about 0.5, while no significant changes in direct flux and single scattering albedo are found. Tropospheric model shows largest differences of diffuse flux around 5–6.5 W m^{-2} with 3.4–4 (%) percent errors.

[62] Table A3 shows the sensitivity test results of surface radiative forcing to the assumed wavelength-independent absorption index ($\bar{m}_i$), surface albedo error, and invariant surface albedo during the day ($\overline{A}$). For surface albedo varying with solar zenith angle change, we applied a second-degree polynomial fit to measured surface albedos at Gosan, Korea. However, the second-degree polynomial fit [$A(\theta_0) = a + b\theta_0^2$, $a = 0.04$, and $b = 1.3 \times 10^{-5}$] was adjusted to produce the average surface albedo of 0.1.

[63] The radiative forcing errors from the use of spectrally invariant imaginary index are mostly within 1 W m^{-2},

Table A3. Error Analysis of Surface Radiative Forcing (F) Induced by Assumed Spectral Independence of Absorption Index ($\overline{m}_i$), and Surface Albedo Error (A = 0.4 With a 0.1 Error Range) and Invariant Surface Albedo With Respect to the Solar Zenith Angle During the Day ($\overline{A} = 0.1$) for AOT = 0.2 and 0.5[a]

	Spectral Dependence, m_i (Albedo = 0.1)			Albedo Error (Albedo = 0.4 ± 0.1)		Albedo Variation		
AOT	m_i (λ)	$\overline{m}_i$	ΔF, %	A = 0.4	ΔF, %	$A(\theta_0)$	$\overline{A}$	ΔF, %
				Soot				
0.2	−46.9	−47.4	0.5 (0.1)	−33.5	4.8 (14)	−48.4	−47.4	1.0 (2.2)
0.5	−96.6	−97.5	0.9 (0.9)	−67.8	10.2 (15)	−100.0	−97.5	2.5 (2.6)
				Urban				
0.2	−28.6	−29.2	0.6 (1.8)	−19.9	3.1 (16)	−29.9	−29.2	0.7 (2.5)
0.5	−63.8	−64.9	1.1 (1.6)	−44.2	7.0 (16)	−66.6	−64.9	1.7 (2.7)
				Troposphere				
0.2	−11.4	−11.5	0.1 (0.7)	−6.2	1.6 (26)	−12.0	−11.5	0.5 (4.4)
0.5	−26.5	−26.7	0.2 (0.7)	−14.9	3.7 (25)	−27.8	−26.7	1.1 (4.3)
				Dust				
0.2	−16.1	−16.8	0.7 (4.4)	−9.8	2.2 (22)	−17.4	−16.8	0.6 (3.7)
0.5	−37.1	−38.9	1.8 (4.8)	−23.5	4.9 (21)	−37.4	−38.9	1.5 (3.9)

[a]Values in parentheses represent respective percentage errors.

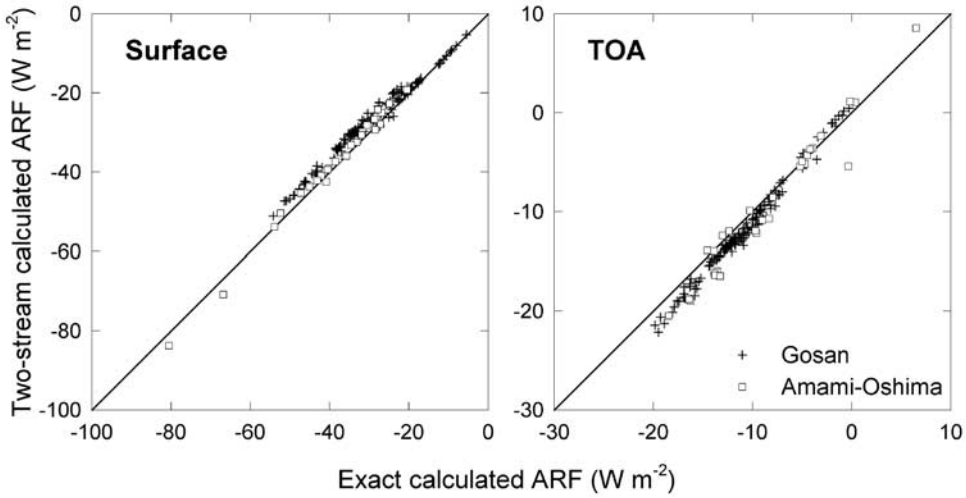

Figure A2. Scatterplots for the comparison of 24-hour averaged radiative forcing (ARF) between exact and two-stream calculations at Gosan (cross hairs) and at Amami-Oshima (squares) during April 2001 at (left) the surface and (right) the TOA.

except for the dust model which shows forcing errors around 1.77 W m^{-2} for larger AOT about 0.5. The uncertainties in surface albedo including the impact of solar zenith angle seem to be elements of inducing uncertain radiative forcing. In conclusion, the uncertainty of aerosol radiative forcing from the assumption of spectral independence can cause errors within about 2% except dust particles whose errors are around 5%.

A2. Two-Stream Approximation

[64] The two-stream approximation is very useful to diagnose what kind of aerosol parameter is important for controlling global and diffuse fluxes at both the surface and the TOA, because the two-stream approximation can separate ARF changes into the contribution by each parameter without a heavy computational burden. In order to calculate the aerosol radiative forcing, taking into account the wavelength dependence of aerosol properties and of incident solar radiation, we use equation (A1) developed by *Russell et al.* [1997]. To estimate the net aerosol radiative forcing at TOA ($\Delta_a F_{TOA}$) under clear sky conditions:

$$\Delta_a F_{TOA} = \mu_0 \int F_T(\lambda) T^2(\lambda, \mu_0) \Delta R(\lambda, \mu_0) d\lambda \qquad \text{(A1)}$$

where F_T is the solar constant, T is the transmissivity of the atmosphere above the aerosol layer. $R \equiv F_{up}/F_{down}$, when downward $\Delta_a F$ can be neglected. In addition, μ_0 is the cosine of the solar zenith angle, λ is wavelength, $\mu_0 F_T(\lambda)$ is the solar spectral irradiance, and ΔR is the change in the surface-atmosphere albedo at the top of the aerosol layer. The net aerosol forcing at the surface ($\Delta_a F_{SFC}$) can be expressed as:

$$\Delta_a F_{SFC} = \mu_0 \int F_T(\lambda) T(\lambda, \mu_0)(1 - R_s)\left(\frac{T_a(\mu_0)}{1 - R_s \overline{R}_a} - 1\right) d\lambda \qquad \text{(A2)}$$

where $R_a(\mu_0)$ and $R_s(\mu_0)$ are the albedo of the aerosol layer and underlying surface, respectively, and $T_a(\mu_0)$ is the transmissivity of the aerosol layer, all for unidirectional radiation incident at zenith cosine μ_0. Overbar denotes an average over the solar zenith angle. The plane albedo and transmission are calculated using the delta-Eddington method [*Meador and Weaver*, 1980].

[65] For the ARF calculation using the two-stream method, wavelength-dependent aerosol parameters and cosine of the solar zenith angle are needed. To avoid the wavelength dependence of the input parameters (thus reducing the number of input parameters) in equations (A1) and (A2), it is useful to find one representative wavelength of input parameters. It was found that the two-stream method, with aerosol parameters at 0.75 μm as inputs, produces an aerosol forcing similar to the exact value. Thus in this sensitivity test, we use aerosol parameters at 0.75 μm to represent the whole spectrum when using the two-stream method.

[66] In order to assess the feasibility of using the two-stream method for testing sensitivity, we computed approximate ARFs using the two-stream method and compared them against the exact calculations at Gosan and Amami-Oshima. The results are shown in Figure A2. The difference between the approximated and exact ARFs tends to increase at both surface and TOA with increased AOT. However, errors in two-stream approximation are around 3 W m^{-2} at both the surface and the TOA, compared to the exact calculation. These results suggest that the two-stream approximation for the TOA and surface ARF can be used to examine how sensitive the ARF is to a chosen aerosol input parameter.

[67] **Acknowledgments.** We express our sincere thanks to B.-C. Choi of the Korean Meteorological Administration for providing data measured at Gosan and to Kuh Kim of Seoul National University for supporting the first author to visit the CCSR. This research has been supported by the Climate Environment System Research Center sponsored by the SRC Program of the Korea Science and Engineering Foundation, by the BK21 Project of the Korean Government, and also by the APEX Project of the Japan Science and Technology Corporation. Part of this research was performed while the first author was hosted by the CCSR as a visiting scientist.

References

Anderson, J. R., P. R. Buseck, T. L. Patterson, and R. Arimoto (1996), Characterization of the Bermuda tropospheric aerosol by combined individual-particle and bulk-aerosol analysis, *Atmos. Environ.*, *30*, 319–338.

Andrews, E., D. Delence, D. Jackson, A. Jefferson, J. Ogren, P. Sheridan, and J. Wendell (2001), *Clim. Monit. Diagn. Lab. Summ. Rep.*, *26*, 60–79.

Bush, B. C., and F. Valero (2003), Surface aerosol radiative forcing at Gosan during the ACE-Asia Campaign, *J. Geophys. Res.*, *108*(D23), 8660, doi:10.1029/2002JD003233.

Chameides, W. L., et al. (1999), Case study of the effects of atmospheric aerosols and regional haze on agriculture: An opportunity to enhance crop yields in China through emission controls, *Proc. Natl. Acad. Sci.*, *96*, 13,626–13,633.

Chuang, P. Y., R. M. Duvall, M. S. Bae, A. Jefferson, J. J. Schauer, H. Yang, J. Z. Yu, and J. Kim (2003), Observations of elemental carbon and absorption during ACE-Asia and implications for aerosol radiative properties and climate forcing, *J. Geophys. Res.*, *108*(D23), 8634, doi:10.1029/2002JD003254.

Chung, C. E., V. Ramanathan, and J. Kiehl (2002), Effects of the south Asian absorbing haze on the northeast monsoon and surface-air heat exchange, *J. Clim.*, *15*, 2462–2476.

Dubovik, O., A. Smirnov, B. N. Holben, M. D. King, Y. J. Kaufman, T. F. Eck, and I. Slutsker (2000), Accuracy assessment of aerosol optical properties retrieved from Aerosol Robotic Network (AERONET) sun and sky radiance measurements, *J. Geophys. Res.*, *105*, 9791–9806.

Dubovik, O., B. N. Holben, T. F. Eck, A. Smirnov, Y. J. Kaufman, M. D. King, D. Tanre, and I. Slutsker (2002a), Variability of absorption and optical properties of key aerosol types observed in worldwide locations, *J. Atmos. Sci.*, *59*, 590–608.

Dubovik, O., B. N. Holben, T. Lapyonok, A. Sinyuk, M. I. Mishchenko, P. Yang, and I. Slutsker (2002b), Non-spherical aerosol retrieval method employing light scattering by spheroids, *Geophys. Res. Lett.*, *29*(10), 1415, doi:10.1029/2001GL014506.

Eck, T. F., B. N. Holben, I. Slutsker, and A. Setzer (1998), Measurements of irradiance attenuation and estimation of aerosol single scattering albedo for biomass burning aerosols in Amazonia, *J. Geophys. Res.*, *103*, 31,865–31,878.

Eck, T. F., B. N. Holben, D. E. Ward, O. Dubovik, J. S. Reid, A. Smirnov, M. M. Mukelabai, N. C. Hsu, N. C. O'Neill, and I. Slutsker (2001), Characterization of the optical properties of biomass burning aerosols in Zambia during the 1997 ZIBBEE field campaign, *J. Geophys. Res.*, *106*, 3425–3448.

Haywood, J. M., and O. Boucher (2000), Estimates of the direct and indirect radiative forcing due to tropospheric aerosols: A review, *Rev. Geophys.*, *38*, 513–543.

Haywood, J. M., and V. Ramaswamy (1998), Global sensitivity studies of the direct radiative forcing due to anthropogenic sulfate and black carbon aerosols, *J. Geophys. Res.*, *103*, 6043–6058.

Haywood, J. M., V. Ramaswamy, and B. J. Soden (1999), Tropospheric aerosol climate forcing in clear-sky satellite observations over the oceans, *Science*, *283*, 1299–1305.

Haywood, J. M., P. N. Francis, M. D. Glew, and J. P. Taylor (2001), Optical properties and direct radiative effect of Saharan dust: A case study of two Saharan outbreaks using data from the U. K. Met Office C-130, *J. Geophys. Res.*, *106*, 18,417–18,430.

Haywood, J. M., P. Francis, S. Osborne, M. Glew, N. Loeb, E. Highwood, D. Tanre, G. Myhre, P. Formenti, and E. Hirst (2003), Radiative properties and direct radiative effect of Saharan dust measured by the C-130 aircraft during SHADE: 1. Solar spectrum, *J. Geophys. Res.*, *108*(D18), 8577, doi:10.1029/2002JD002687.

Hess, M., P. Koepke, and I. Schult (1998), Optical properties of aerosols and clouds: The software package OPAC, *Bull. Am. Meteorol. Soc.*, *79*, 831–844.

Higurashi, A., and T. Nakajima (2002), Detection of aerosol types over the East China Sea near Japan from four-channel satellite data, *Geophys. Res. Lett.*, *29*(17), 1836, doi:10.1029/2002GL015357.

Higurashi, A., T. Nakajima, B. N. Holben, A. Smirnov, R. Frouin, and B. Chatenet (2000), A study of global aerosol optical climatology with two channel AVHRR remote sensing, *J. Clim.*, *13*, 2011–2027.

Huebert, B. J., T. Bates, P. B. Russell, G. Shi, Y. J. Kim, K. Kawamura, G. Carmichael, and T. Nakajima (2003), An overview of ACE-Asia: Strategies for quantifying the relationships between Asian aerosols and their climatic impacts, *J. Geophys. Res.*, *108*(D23), 8633, doi:10.1029/2003JD003550.

Intergovernmental Panel on Climate Chang (IPCC) (2001), *Climate Change 2001: The Scientific Basis*, edited by J. T. Houghton et al., 881 pp., Cambridge Univ. Press, New York.

Jacobson, M. Z. (2001), Strong radiative heating due to the mixing state of black carbon in atmospheric aerosols, *Nature*, *409*, 695–697.

Kim, D. (2003), Aerosol optical properties and associated radiative forcing over east Asia determined from ground-based Sun photometry measurements, Ph.D. dissertation, 122 pp., School of Earth and Environ. Sci., Seoul Natl. Univ., Seoul.

Kim, D., B. Sohn, T. Nakajima, T. Takamura, T. Takemura, B. Choi, and S. Yoon (2004), Aerosol optical properties over east Asia determined from ground-based sky radiation measurements, *J. Geophys. Res.*, *109*, D02209, doi:10.1029/2003JD003387.

King, M. D., and B. M. Herman (1979), Determination of the ground albedo and the index of absorption of atmospheric particulates by remote sensing. part I: Theory, *J. Atmos. Sci.*, *36*, 163–173.

Kneizys, F. X., E. P. Shettle, L. W. Abreu, J. H. Chetwynd, G. P. Anderson, W. O. Gallery, J. E. A. Selby, and S. A. Clough (1988), *Users Guide to LOWTRAN 7*, *Rep. AFGL-TR-88–0177*, 137 pp., Air Force Geophys. Lab., Bedford, Mass.

Liao, H., and J. H. Seinfeld (1998), Radiative forcing by mineral dust aerosols: Sensitivity to key variables, *J. Geophys. Res.*, *103*(D24), 31,637–31,646.

Markowicz, K. M., P. J. Flatau, P. K. Quinn, C. M. Carrico, M. K. Flatau, A. M. Vogelmann, D. Bates, M. Liu, and M. J. Rood (2003), Influence of relative humidity on aerosol radiative forcing: An ACE-Asia experiment perspective, *J. Geophys. Res.*, *108*(D23), 8662, doi:10.1029/2002JD003066.

Meador, W. E., and W. R. Weaver (1980), Two-stream approximations to radiative transfer in planetary atmosphere: A unified description of existing methods and a new improvement, *J. Atmos. Sci.*, *37*, 630–643.

Michalsky, J. J., L. C. Harrison, and W. E. Berkheiser III (1995), Cosine response characteristics of some radiometric and photometric sensors, *Sol. Energy*, *54*, 397–402.

Myhre, G., A. Grini, J. M. Haywood, F. Stordal, B. Chatenet, D. Tanre, J. Sundet, and I. Isaksen (2003), Modeling the radiative impact of mineral dust during the Saharan Dust Experiment (SHADE) campaign, *J. Geophys. Res.*, *108*(D18), 8579, doi:10.1029/2002JD002566.

Nakajima, T., and M. Tanaka (1986), Matrix formulations for the transfer of solar radiation in a plane-parallel scattering atmosphere, *J. Quant. Spectrosc. Radiat. Transfer*, *35*, 13–21.

Nakajima, T., and M. Tanaka (1988), Algorithms for radiative intensity calculations in moderately thick atmospheres using a truncation approximation, *J. Quant. Spectrosc. Radiat. Transfer*, *40*, 51–69.

Nakajima, T., G. Tonna, R. Rao, R. Boi, Y. Kaufman, and B. Holben (1996a), Use of sky brightness measurements from ground for remote sensing of particulate polydispersions, *Appl. Opt.*, *35*, 2672–2686.

Nakajima, T., T. Hayasaka, A. Higurashi, G. Hashida, N. Moharram-Nejad, Y. Najafi, and H. Valavi (1996b), Aerosol optical properties in the Iranian region obtained by ground-based solar radiation measurements in the summer of 1991, *J. Appl. Meteorol.*, *35*, 1265–1278.

Nakajima, T., et al. (2003), Significance of direct and indirect radiative forcings of aerosols in the East China Sea region, *J. Geophys. Res.*, *108*(D23), 8658, doi:10.1029/2002JD003261.

Ohta, S., K. Ryo, M. Naoto, and Y. Sadamu (2002), Measurements of optical and chemical properties of atmospheric aerosols at Fukue and Amami-Oshima Islands, paper presented at Fifth APEX International Workshop, Jpn. Space and Technol. Corp., Miyazaki, Japan, 3–5 June 2002.

Ramanathan, V., P. J. Crutzen, J. T. Kiehl, and D. Rosenfeld (2001a), Aerosol, climate, and hydrological cycle, *Science*, *294*, 2119–2124.

Ramanathan, V., et al. (2001b), Indian Ocean Experiment: An integrated analysis of the climate forcing and effects of the great Indo-Asian haze, *J. Geophys. Res.*, *106*, 28,371–28,398.

Russell, R. B., S. A. Kinne, and R. W. Bergstrom (1997), Aerosol climate effects: Local radiative forcing and column closure experiments, *J. Geophys. Res.*, *102*, 9397–9407.

Satheesh, S. K., and V. Ramanathan (2000), Large differences in the tropical aerosol forcing at the top of the atmosphere and Earth's surface, *Nature*, *405*, 60–63.

Satheesh, S. K., V. Ramanathan, X.-L. Jones, J. M. Lobert, I. A. Podgorny, J. M. Prospero, B. N. Holben, and N. G. Loeb (1999), A model for the natural and anthropogenic aerosols over the tropical Indian Ocean derived from Indian Ocean Experiment data, *J. Geophys. Res.*, *104*, 27,421–27,440.

Shettle, E. P., and R. W. Fenn (1979), Models for the aerosols of the lower atmosphere and the effects of humidity variations on their optical properties, *Rep. AFGL-TR-79-0214*, 94 pp., Air Force Geophys. Lab., Hanscom Air Force Base, Mass.

Sugimoto, N., A. Shimizu, and I. Matsui (2002), Observations of aerosols and clouds with lidars, paper presented at Fifth APEX International Workshop, Jpn. Space and Technol. Corp., Miyazaki, Japan, 3–5 June 2002.

Takemura, T., I. Uno, T. Nakajima, A. Higurashi, and I. Sano (2002), Modeling study of long-range transport of Asian dust and anthropogenic aerosols from east Asia, *Geophys. Res. Lett.*, *29*(24), 2158, doi:10.1029/2002GL016251.

Takeuchi, N., T. Takamura, and T. Nakajima (1999), Continuous monitoring data of micro pulse lidar and radiation data at Si Samrong radiation observation station, Sukhothai, Thailand, *Rep. 1997.7–1998.1*, 190 pp., Cent. for Environ. Remote Sens., Chiba Univ., Chiba, Japan.

Tanre, D., Y. J. Kaufman, B. N. Holben, B. Chatenet, A. Karnieli, F. Lavenu, L. Blarel, O. Dubovik, L. A. Remer, and A. Sminov (2001), Climatology of dust aerosol size distribution and optical properties derived from remotely sensed data in the solar spectrum, *J. Geophys. Res.*, *106*, 18,205–18,217.

Tsuruta, H., et al. (2003), Characterization, source identification, and optical properties of atmospheric aerosols measured at Amami-Oshima, southwest Japan, during spring seasons under the APEX field campaign program, *JST/CEREST/APEX 2003 Interim Rep.*, pp. 21–40, Jpn. Sci. and Technol. Corp., Saitama, Japan.

D.-H. Kim, Scripps Institution of Oceanography, University of California, San Diego, 9500 Gilman Drive, La Jolla, CA 92093-0221, USA. (dkim@fiji.ucsd.edu)

T. Nakajima, Center for Climate System Research, University of Tokyo, 4-6-1 Komaba, Meguro-ku, Tokyo 153-8904, Japan. (teruyuki@ccsr.u-tokyo.ac.jp)

B. J. Sohn, School of Earth and Environmental Sciences, Seoul National University, NS80, Seoul 151-747, Korea. (sohn@snu.ac.kr)

T. Takamura, Center for Environmental Remote Sensing, Chia University, 1-33 Yayoi-cho, Inage-ku, Chiba 263-8522, Japan. (takamura@ceres.cr.chiba-u.ac.jp)